JMEPEG (2019) 28:6391–6406
https://doi.org/10.1007/s11665-019-04365-9

©ASM International
1059-9495/$19.00

Microstructural Development and Mechanical Properties of Friction Stir Welded Ferritic Stainless Steel AISI 409

M.M.Z. Ahmed, Mohamed M. El-Sayed Seleman, Mostafa Shazly, Moataz M. Attallah, and Essam Ahmed

(Submitted August 19, 2018; in revised form May 28, 2019; published online October 10, 2019)

This work investigates the effect of friction stir welding process parameters (rotation rate and traverse speed) on the microstructural evolution of friction stir welded (FSWed) ferritic stainless steel (FSS) AISI 409. Optical microscope, scanning electron microscope and electron backscattering diffraction are used to quantitatively assess the development in grain structure and texture. The microstructural development suggested that thermo-mechanical deformation occurs in the stir zone within the austenite/ferrite phase region, ultimately transforming upon cooling into bainitic/ferritic microstructure. The fraction and size of the bainitic/ferritic grains are found to vary through the thickness of the joints. High fractions of coarse ferritic grains are found near the top of the stir zone, and low fraction of fine ferritic grains is found near the bottom of the stir zone. This bainitic/ferritic grain structure resulted in an increase in the hardness of the stir zone by about 74% relative to the base material. The tensile strength of the FSWed FSS joints is almost at the same level of the base material with reduction in the ductility as a result of the increased hardness of the weld zone.

Keywords EBSD, ferritic stainless steel, friction stir welding, microstructure, mechanical properties

1. Introduction

Ferritic stainless steels (FSSs) are Fe-C-Cr alloys, containing 10.5-30 wt.% Cr, up to 0.2 wt.% C, and minor additions of ferrite promoters such as Al, Nb, Ti and Mo (Ref 1). When compared to austenitic stainless steels (ASSs), FSSs are less expensive, have lower thermal expansion coefficient and better resistance to stress corrosion cracking (Ref 2, 3). Due to these properties, FSSs have been widely used in different components of automotive exhaust systems (Ref 2, 4). However, in conventional fusion welding processes, FSSs suffer from grain coarsening in the heat-affected zone (HAZ) and fusion zone (FZ), leading to reduction in toughness, ductility and corrosion resistance of the welded joints (Ref 2). Grain coarsening in HAZ can be hindered by using low heat input in fusion welding to keep grain growth as localized as possible and suppress sensitization (Ref 5). Alternatively, a localized low heat input can be introduced by using friction stir welding (FSW) process, the recently developed solid-state joining technology (Ref 6-17), that was successfully used to weld FSSs (Ref 2) and other high-temperature materials (Ref 7). Moreover, low heat input is likely to result in low residual stresses and eliminate solidification defects. However, FSW of ferritic stainless steels is a more complex process than that of aluminum alloys due to the occurrence of phase transformation (Ref 6, 11, 18-20). This phase transformation process is affected by the thermo-mechanical cycle during FSW process and results from the interaction of many process parameters, such as tool design (Ref 11, 13, 14), axial load (Ref 21), tool rotation rate (Ref 6, 16), welding travel speed (Ref 22), plunge depth (Ref 23) and tool tilt angle (Ref 24).

Early attempt on FSW of stainless steels was conducted by Thomas et al. (Ref 25) in 2009. They made an attempt on FSW of a ferritic–martensitic, low carbon, 12 wt.% Cr stainless alloys with traverse speed s in the range of 102-240 mm/min. The maximum temperature reported during welding was 1100 °C, and higher hardness values were obtained in the HAZ. Since then, several studies on FSW have emerged for similar and dissimilar stainless steel plates. For example, on 409 FSS, Cho et al. (Ref 23) were able to produce fine-grained microstructure in the SZ with high fraction of low-angle grain boundaries (LAGB) which were found to increase with increasing the plunging depth. Lakshminarayanan and Balasubramanian (Ref 26) studied the effect of tool rotational speed, travel speed and tool shoulder diameter on the quality of welded joints in AISI 409 FSS. They found the travel speed to be the most significant parameter followed by tool rotational speed and then the tool shoulder diameter. In another study on the same alloys, Lakshminarayanan and Balasubramanian (Ref 27) found that increasing the plunge depth generates severe plastic deformation in the SZ, which leads to grain refinement, and an enhancement in the fatigue strength and the fatigue crack growth resistance. Also, Salemi Golezani et al. (Ref 28) studied the FSW of AISI 430 FSS and reported that grain

M.M.Z. Ahmed, Mechanical Engineering Department, The British University in Egypt, Al-Sherouk, Cairo 11837, Egypt; Suez and Sinai Metallurgical and Materials Research Center of Scientific Excellence (SSMMR-CSE), Suez University, Suez 43511, Egypt; and Metallurgical and Materials Engineering Department, Faculty of Petroleum and Mining Engineering, Suez University, Suez 43511, Egypt; **Mohamed M. El-Sayed Seleman** and **Essam Ahmed**, Suez and Sinai Metallurgical and Materials Research Center of Scientific Excellence (SSMMR-CSE), Suez University, Suez 43511, Egypt; and Metallurgical and Materials Engineering Department, Faculty of Petroleum and Mining Engineering, Suez University, Suez 43511, Egypt; **Mostafa Shazly**, Mechanical Engineering Department, The British University in Egypt, Al-Sherouk, Cairo 11837, Egypt; **Moataz M. Attallah**, School of Metallurgy and Materials, University of Birmingham, Edgbaston, Birmingham B15 2TT, UK. Contact e-mail: mohamed.elnagar@suezuniv.edu.eg.

refinement in the nugget (NG) achieved by dynamic recrystallization and increasing heat input through higher rotational speed at constant travel speed to produce more grain refinement the NG. Similarly, in 18Cr-2Mo FSS, Han et al. (Ref 29) reported grain refinement in NG with increasing the travel speed while maintaining a constant tool rotation rate. Bilgin and Meran (Ref 30) reported an improvement in the notch impact resistance of FSWed AISI 430 FSSs by increasing the travel speed and decreasing the tool rotation rate. This could be directly related to the microstructural development upon FSW at different welding parameters. Thus, the present work aims to investigate the microstructural evolution of FSWed AISI 409 FSS and correlate the resulting microstructure with the mechanical properties of the FSWed joints.

2. Experimental Work

2.1 Material and FSW Parameters

In the present work, 4-mm-thick AISI 409 FSS plates, of chemical composition 10.74% Cr, 0.68%Mn, 0.52%Si and 0.02%C (in wt.%), were used to produce three FSWed butt joints with no shielding gas. FSW machine shown in Fig. 1(a) has a 22 kW power, 3000 rpm max spindle speed, 1000 mm/min max traverse speed, 100 kN max vertical force, and a tilting head of $\pm$ 5° is used to carry out the welding process. The WC tool used in this work, shown in Fig. 1(b) and (c), has a probe length, diameter and shoulder diameter of 3.8, 5 and 18 mm, respectively. Ahmed et al. (Ref 31) reported that WC tool exhibited no wear and high dimension stability after FSW experiments of TWIP steel sheets. Three welds were produced using tool rotational speeds of 1000 and 1500 rpm and traverse speeds of 100 and 150 mm/min. After FSW, the joints were sectioned normal to the welding direction (WD) for the subsequent characterizations.

2.2 Microstructure Characterization

The base material (BM) and the FSWed materials were investigated using optical microscope (OM), following metallographic preparation by SiC grinding, diamond polishing and final mechanical polishing using 0.05-µm alumina particles. The samples were etched using an etchant composed of 5 g $CuCl_2$ + 100 ml HCl + 100 ml C_2H_5OH. Then, samples were investigated using a Quanta FEG 250 scanning electron microscope.

Electron backscattered diffraction (EBSD) was used for microstructure characterization of the polished samples. The acquisition of the EBSD data was carried out using a fully automated EDAX-EBSD system in a Quanta FEG 250 SEM equipped with Hikari EDAX-EBSD camera, controlled by Orientation Imaging Microscopy Data Collection software (OIM DC 7.2), operating at 20 kV. The selection of the EBSD data acquisition step size was based on the rough grain size identified using OM. The BM and the center of the SZ of the 1000 rpm, 100 and 150 mm/min weld were investigated using 1-µm step size to pick up the orientations of as many grains as possible, such that the crystallographic texture can be represented with a reasonable statistical confidence. High-resolution EBSD maps were also acquired at step sizes of 0.25 and 0.05 µm at the center of the joints to capture the fine and the ultrafine grains. In all cases, a minimum indexing rate of 80% was obtained, with a high confidence index $>$ 0.4.

2.3 Mechanical Properties Characterization

The mechanical properties of the FSWed butt joints were characterized in terms of tensile and hardness properties. A computerized universal testing machine (Instron 4208, with a 300-kN load cell) was used to conduct the tensile tests at a constant crosshead speed of 5×10^{-2} mm s^{-1}. Sub-size tensile test samples were machined according to ASTM E8 M-04, with the weld zone positioned at the gauge length of the sample. Vickers hardness tester, model HWDV-7S, with a load of 2 kgf and a holding time of 15 s was used to evaluate the hardness of the joints. Vickers hardness measurements at a step of 0.5 mm along the weld cross section were performed to obtain hardness profile across the different weld zones.

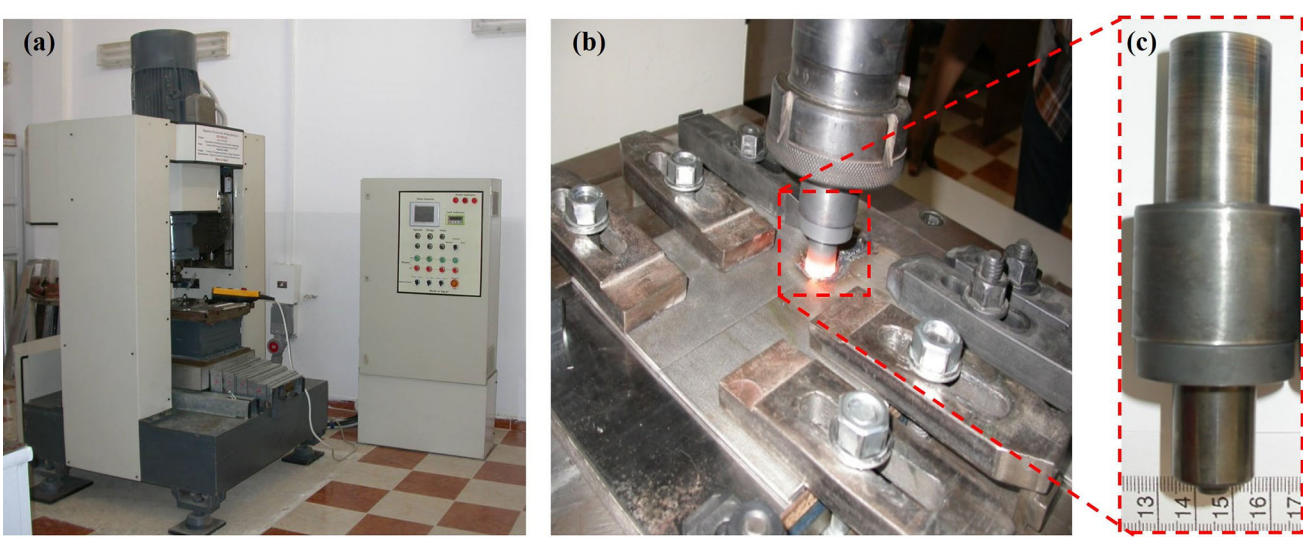

Fig. 1 (a) An image of the FSW machine used in this work, (b) the experimental setup during FSW and (c) WC tool installed in the tool steel holder before FSW

3. Results and Discussion

3.1 Base Material Microstructure Analysis

Figure 2(a) and (b) shows the optical and SEM micrographs for the as-received FSS BM, respectively. The BM exhibits a microstructure of elongated ferrite grains along the rolling direction (RD) (Fig. 2a), with the carbides distributed mainly at the grain boundaries and less frequently scattered within the ferrite grains (Fig. 2b). Figure 2 from (c) to (i) shows the EDS analysis of the grain boundaries in a selected area of the BM. The results clearly confirm the presence of (Mn-Cr)-containing carbides at the grain boundaries.

Figure 3(a) shows the orientation imaging map (OIM) of the FSS BM using inverse pole figure (IPF) coloring with respect to the rolling direction (RD). The map shows near horizontally aligned ferrite grains with random orientation in general. The grain structure is relatively fine with an average grain size of 8 μm, as shown in the grain size distribution histogram in Fig. 3(c). Nonetheless, the grain size ranges between 4 μm and 22 μm, demonstrating a rather slightly elongated morphology. The corresponding grain boundary (GB) map of the BM is shown in Fig. 3(b) where the high-angle boundaries (HABs) > 15° are represented by black lines, whereas the low-angle boundaries (LABs) of 5-15° are represented by red lines. The map shows high density of LABs which is also observed from the misorientation angle distribution histogram in Fig. 3(d). This high density of LABs indicates that the base material is in a deformed state. The PFs illustrated in Fig. 3(e) show a typical bcc metals' simple shear deformation texture (Ref 32).

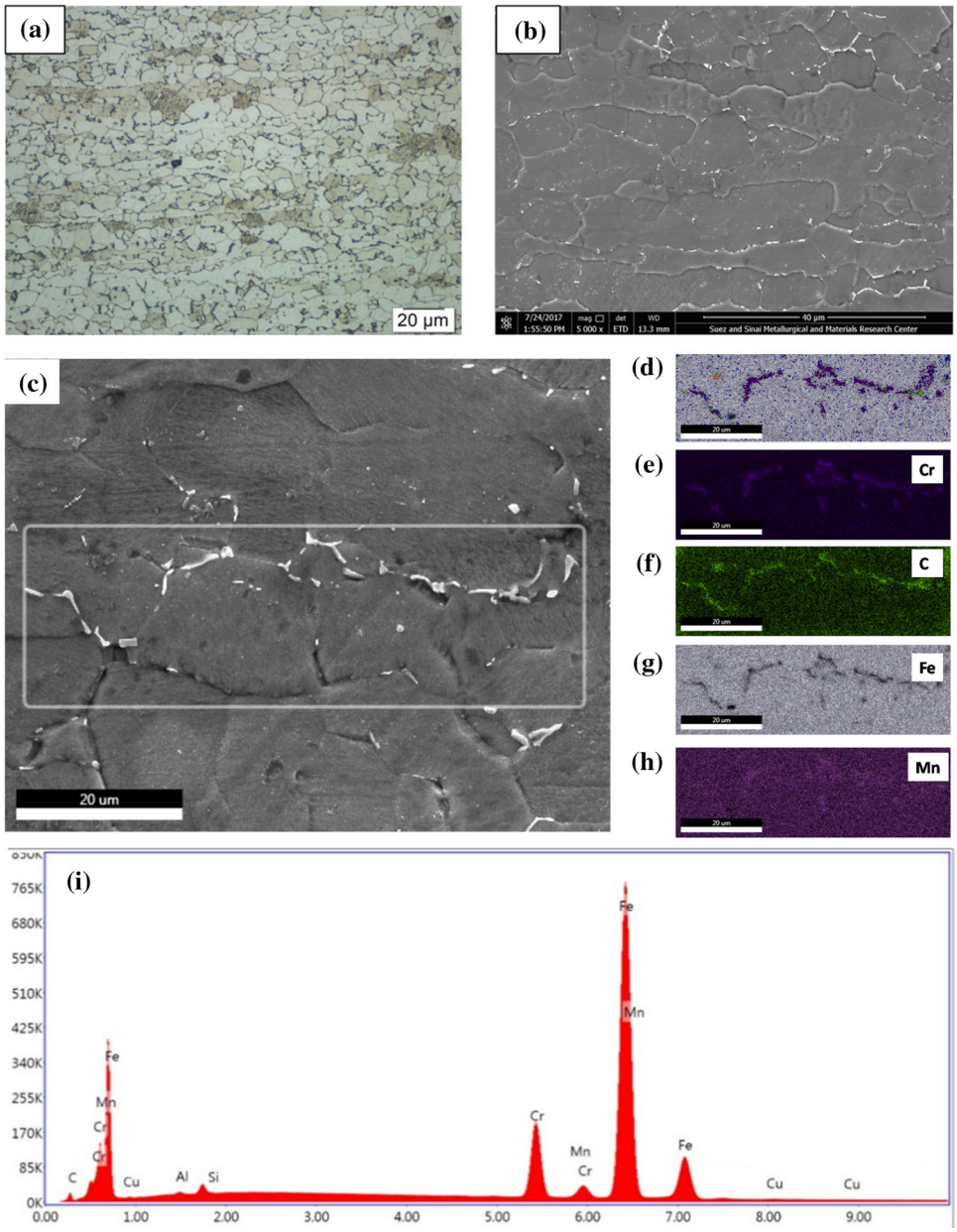

Fig. 2 (a) Optical and (b) SEM micrographs showing the microstructure of the BM, (c) selected area for EDS analysis, (d-h) elemental maps and (i) elemental chart of the selected area in (c)

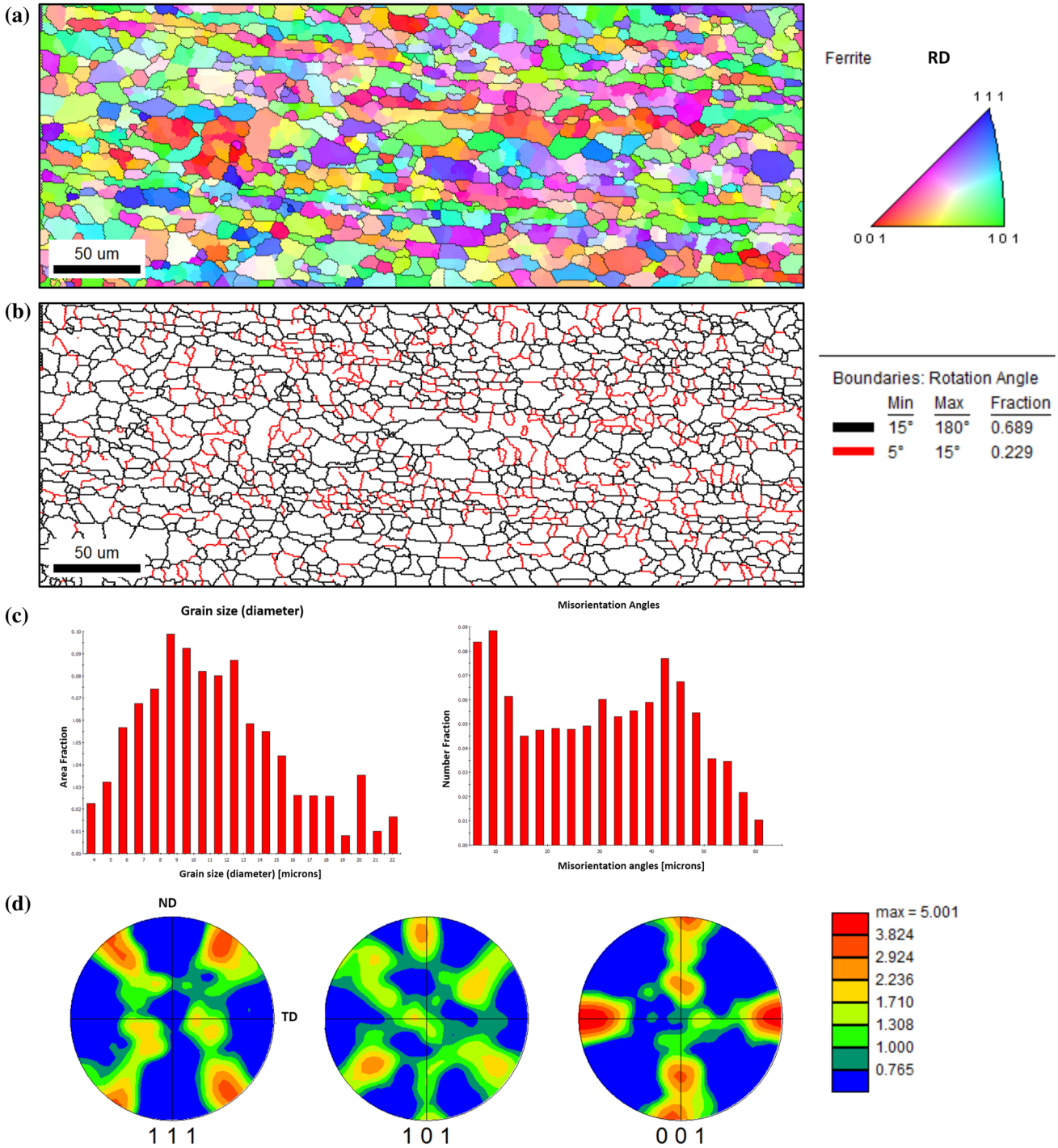

Fig. 3 (a) EBSD map of the FSS BM using IPF colors with respect to the RD, (b) grain boundary map with the HABs > 15° in black lines and the LABs 5-15° in red lines, (c) grain size distribution, (d) misorientation angle distribution, (e) 111, 101 and 001 pole figures. The IPF coloring triangle used throughout the paper is shown to the right of the IPF map in (a) (Color figure online)

3.2 Friction Stir Welded FSS Joints

3.2.1 Microstructural Development. Figure 4 shows the optical macrographs for the transverse cross section of the FSS butt joints welded using different FSW conditions. It is noted that the weld zones appear as arc-like shape facing toward the shoulder of the tool which includes the nugget (NG) zone and the thermo-mechanically affected zone (TMAZ), with diffusive interface between the NG and the TMAZ. This can be attributed to the phase transformation taking place in stainless steel due to the thermal cycle experienced by both zones during FSW. The macrographs show defect-free joints at the examined FSW parameters. The weld zone can be distinguished from the BM after etching by its lighter dark color relative to the dark BM due to the microstructural differences. Within the weld zone, dark bands are observed in the NG where they are hardly

visible in the joint produced by 1000 rpm rotational rate and 100 mm/min traverse speed (Fig. 4a). These dark bands become more marked and larger in size with increasing rotational rate and traverse speed as shown in Fig. 4(b) and (c). These regions are not affected by the etching process and appeared dark on the macrographs while appeared lighter under the optical microscope.

It is known that the microstructure development in the weld zones is directly related to the thermo-mechanical deformation experienced during FSW. The amounts of heat and deformation generated during FSW under the shoulder have contributions from both the probe and the shoulder of the tool, while near the backing plate has only probe contribution (Ref 33). Accordingly, a variation in the microstructure through the thickness of the joint from the top to the bottom of the weld zone is expected. Furthermore, FSW parameters such as the tool rotation rate and traverse speed have a significant effect in the amount of heat generated during FSW. The microstructure of the FSS butt joints is investigated near the top and near the bottom of the weld zones, and their microstructures are given in Fig. 5 and 6, respectively. The microstructure near the top of the weld zone shown in Fig. 5(a), (b) and (c) clearly consists of bainitic/ferritic grain structure. The ferritic grains are relatively coarse with bright color, whereas the bainitic ferrite grains are finer with relatively darker color. The coarse ferrite grains more likely represent the pro-ferrite grains, whereas the bainitic ferrite grains formed upon continuous cooling from the austenite phase (Ref 32). This suggests that the deformation process took place in the ferrite–austenite phase field where, upon heating, the BM original microstructure transforms into ferrite–austenite phase and experiences plastic deformation during FSW. Upon cooling, the austenite phase transforms into bainitic ferrite due to rapid cooling and high shear strain (Ref 34). It has been reported that bainite occurs during thermal treatments at cooling rates that are high enough for pearlite to form, yet not rapid enough to produce martensite (Ref 32). It can be observed that the relative fraction and size of the coarse grains increase by increasing the tool rotation rate from 1000 to 1500 rpm (Fig. 5a and c). This highlights the significant effect of the tool rotation rate on the weld zone microstructure.

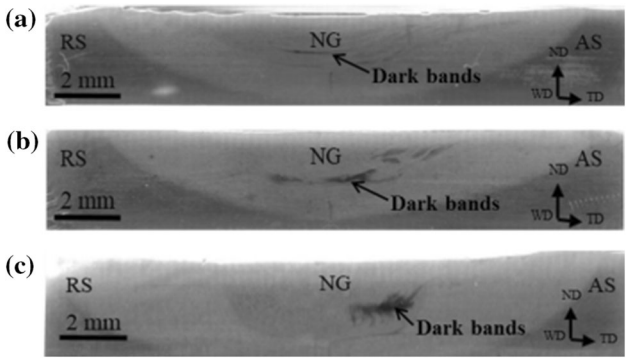

Fig. 4 Optical macrographs for the transverse cross section of the FSS FSW joints, welded at (a) 1000 rpm, 100 mm/min, (b) 1000 rpm, 150 mm/min, and (c) 1500 rpm, 150 mm/min

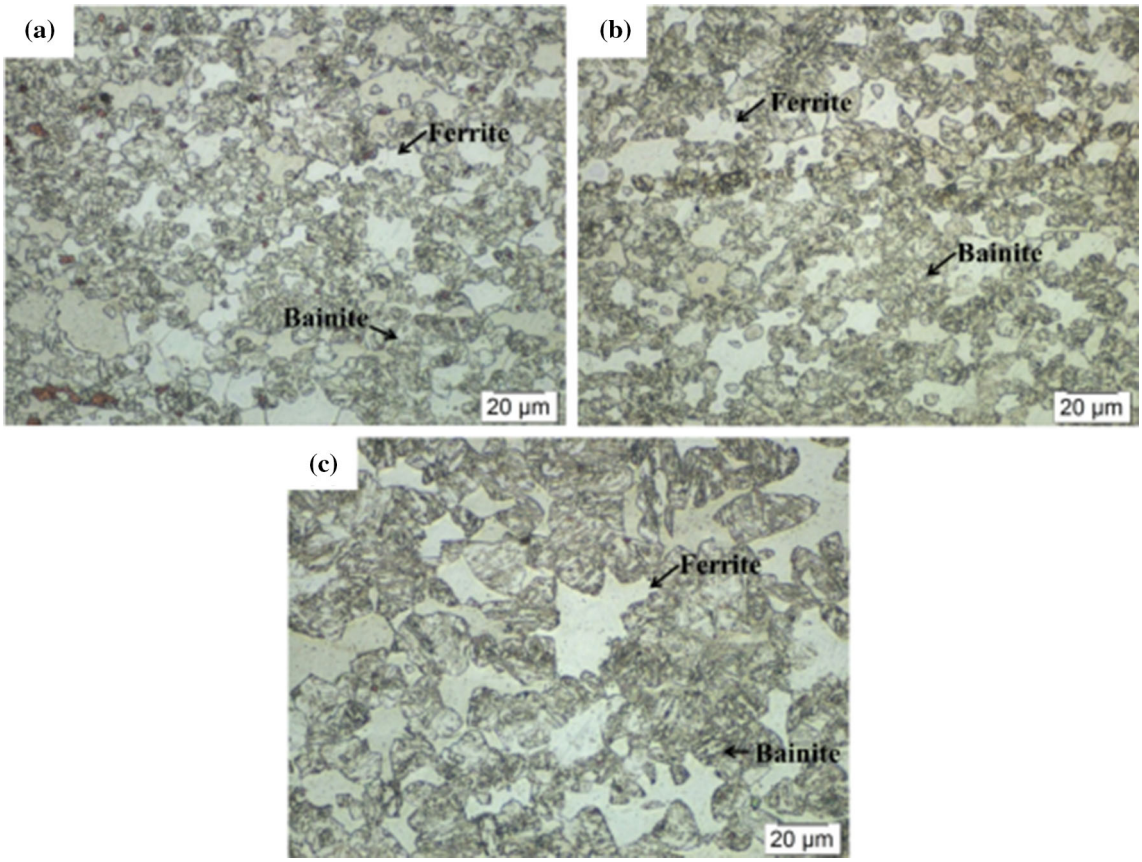

Fig. 5 Optical micrographs showing the microstructure near the top of the NG of the FSS joints (a) 1000 rpm, 100 mm/min, (b) 1000 rpm, 150 mm/min, and (c) 1500 rpm, 150 mm/min

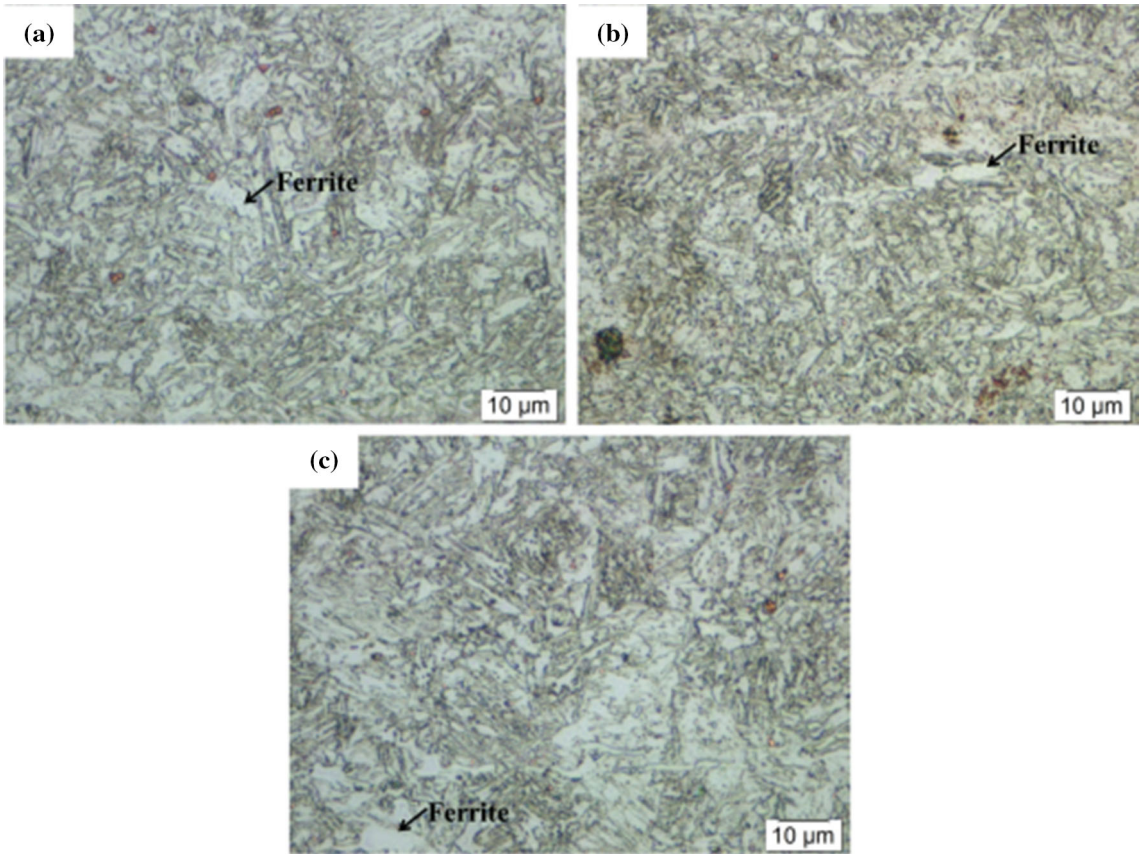

Fig. 6 Optical micrographs showing the microstructure near the bottom of the NG of the FSS joints (a) 1000 rpm, 100 mm/min, (b) 1000 rpm, 150 mm/min, and (c) 1500 rpm, 150 mm/min

Moreover, the microstructure near the bottom of the weld zone (Fig. 6) shows a mixture of fine ferrite grains and bainitic ferrite grains. This can be attributed to the low heat input near the bottom of the weld zone in addition to the high cooling rate due to its proximity to the backing plate. Both factors have resulted in a microstructure significantly finer near the base of the weld zone.

The preferentially etched dark regions in the weld zone observed in the macrographs in Fig. 4 are also investigated using OM and SEM to confirm that they do not contain any structural defects. Figure 7 shows the microstructure of this region, which appears to consist of high-density deformation ferritic bands, which were previously observed in FSW of Cr-Mn-Mo-N austenitic stainless steel (Ref 34), high nitrogen nickel-free austenitic stainless steel (Ref 35) and single-crystal austenitic stainless steel (Ref 36). However, Mahmoudiniya et al. (Ref 37) reported that the formation mechanism of the ferritic layer is not yet fully understood. These elongated banded microstructures in the stir zone are likely to be related to the stabilization of ferrite due to the micro-segregation of FSS alloying elements.

SEM investigation of the microstructure within the weld indicates that the process resulted in the dissolution of the carbide particles observed along the grain boundaries in the BM. This can be observed from the SEM micrograph shown in Fig. 8 with the corresponding EDS elemental maps (Fig. 8c, d, e, and f) for the analyzed insets in Fig. 8(a) and (b). This result suggests that the thermal cycle experienced during FSW, in terms of the peak temperature, is high enough to dissolve the carbide particles and also the cooling rate is rapid enough to prevent their formation upon cooling. In addition, the microstructure in the HAZ shows the existence of carbide particles, as shown in the SEM micrographs in Fig. 9(a) and (b) with the corresponding EDS elemental maps in Fig. 9 from (c) to (f). Furthermore, the grain size distribution within the HAZ also resembles that of the BM. This suggests that the microstructure is mildly affected by the thermal field within the HAZ as noted previously by Bhadeshia and Honeycombe (Ref 33).

3.2.2 EBSD Grain Structure and Texture. Figure 10(a) and (b) shows the IPF orientation imaging maps of FSS FSW joints welded at a rotation speed of 1000 rpm and different travel speeds of 100 and 150 mm/min, respectively, with the HABs $> 15°$ superimposed on them. In terms of the crystallographic orientation, the maps show a mixture of the three $\langle 111 \rangle$ (blue), $\langle 001 \rangle$ (red) and $\langle 110 \rangle$ (green) orientations. In terms of the grain structure, it can be noted that the weld at low traverse speed of 100 mm/min exhibited a dual-phase structure of coarse ferrite grains and fine bainitic ferrite grains as shown in Fig. 6(a). This bainitic/ferritic microstructure has been observed in the stir zone center of the FSWed micro-alloyed steel (Ref 33). Increasing the traverse speed to 150 mm/min at a constant rotation rate has resulted in a significant reduction in

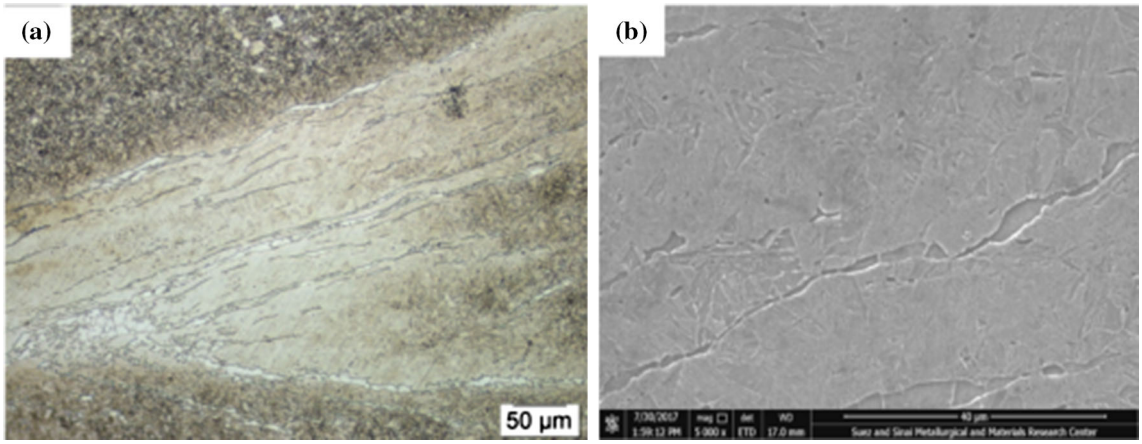

Fig. 7 (a) OM and (b) SEM micrographs for the dark regions observed in the weld macrographs (Fig. 4)

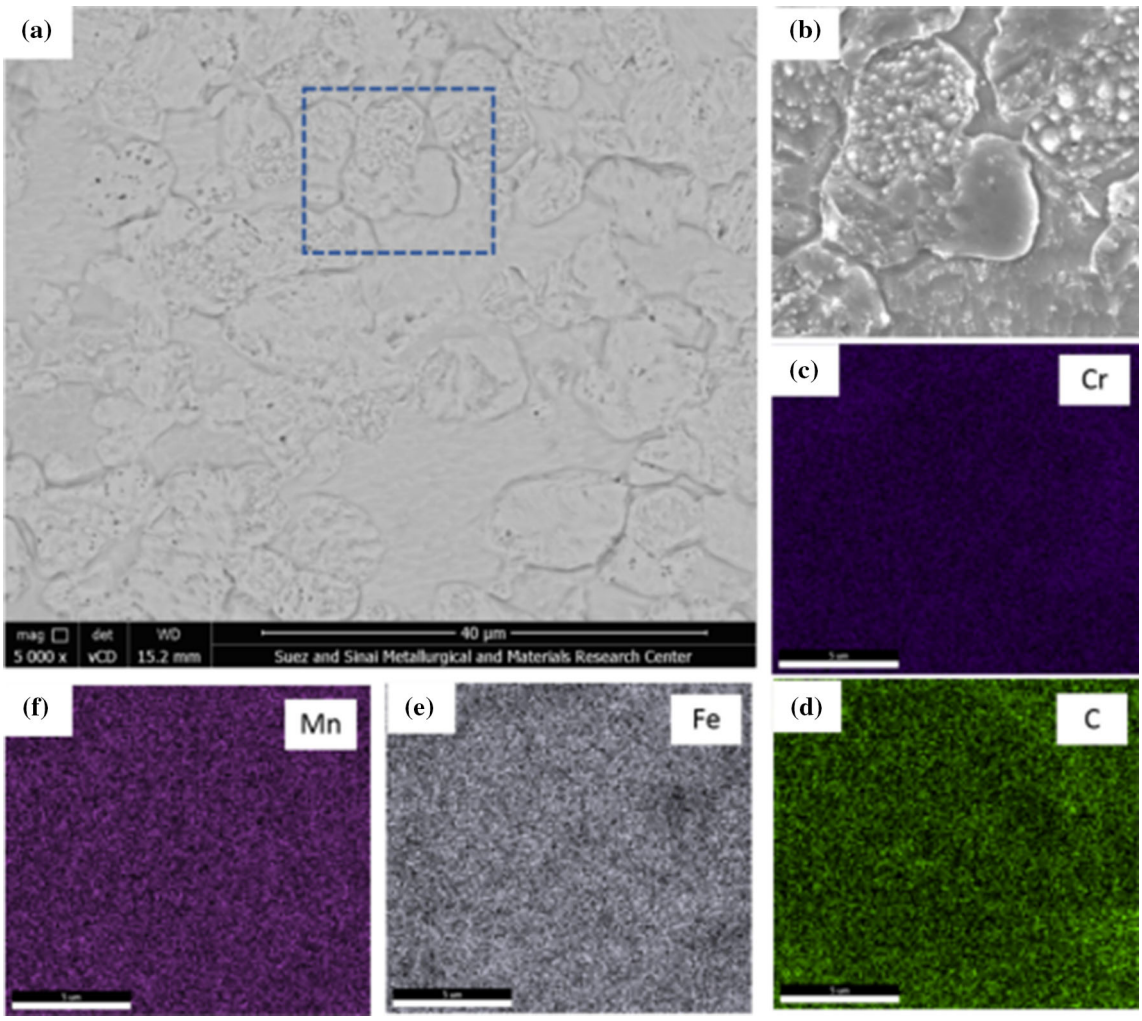

Fig. 8 (a) and (b) SEM micrographs of the NG of the FSS joint welded at 1000 rpm and 100 mm/min and (c-f) elemental maps of NG selected area

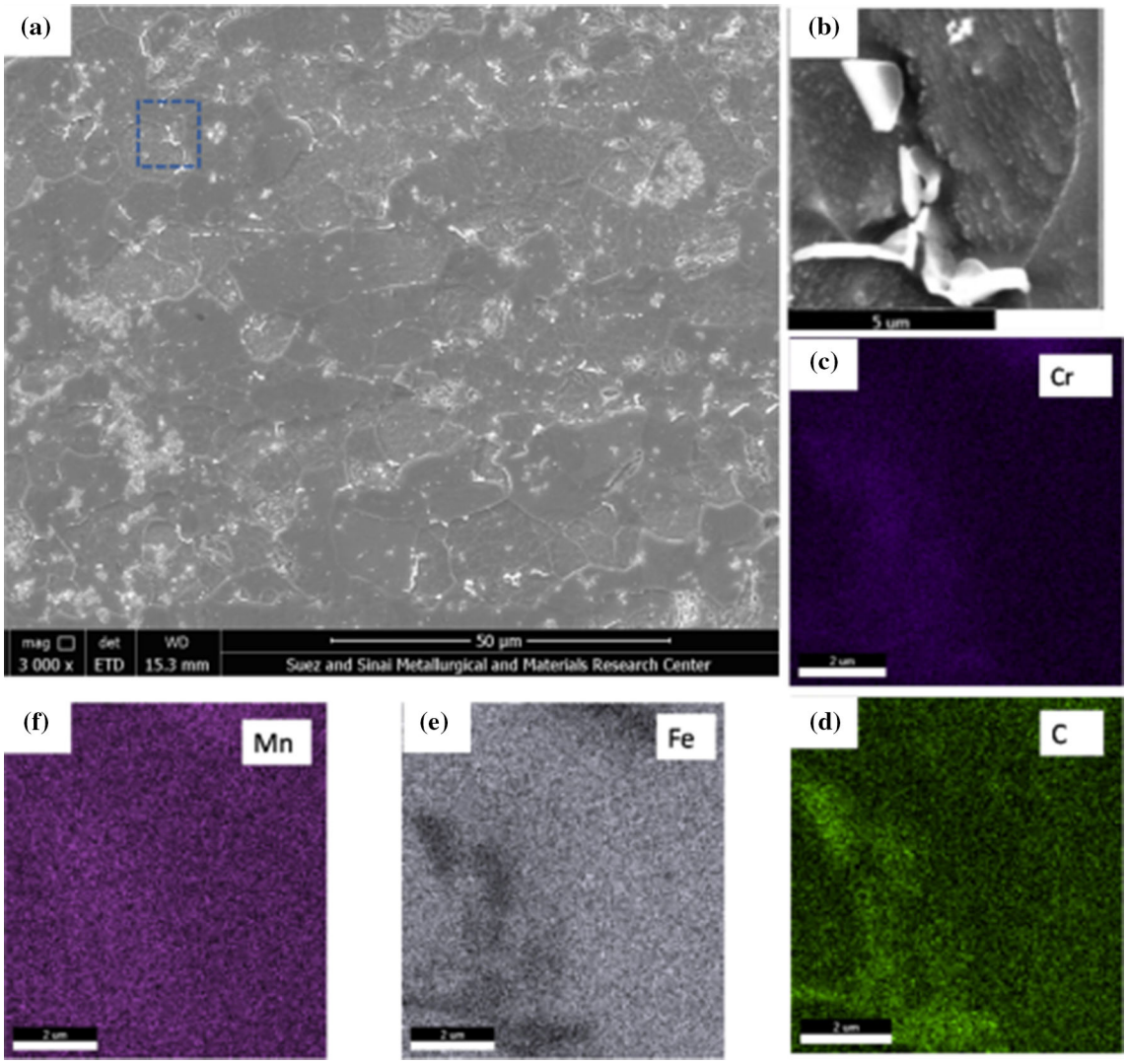

Fig. 9 (a) and (b) SEM micrographs of the HAZ of the FSS joint welded at 1000 rpm and 100 mm/min and (c-f) elemental maps of NG selected area

the ferrite grains fraction, with the grain structure being mainly dominated by the fine bainitic. Similarly, an increase in the fraction of ferrite grains toward the edges of the NG zone has been noted by Rahimi et al. (Ref 33). This can be attributed to the thermal cycle experienced in each weld. The main parameters of the thermal cycle that affect the microstructural development in the SZ are the peak temperature and the cooling rate (Ref 33, 38). FSW at high speed using the same rotation rate reduced the thermal cycle period and the peak temperature (Ref 38).

Grain boundary maps of the two welds with HABs $> 15°$ in black lines and LABs $> 5°$ in red lines are shown in Fig. 11. The GB maps consist of two types of grains: large grains that are almost free of substructures, indicating that these grains are formed due to continuous dynamic recrystallization, and fine grains with high density of substructures which represent the bainitic ferrite grains. Figure 12 shows the grain size and misorientation angle distributions of the FSWed FSS joints at a constant rotation rate of 1000 rpm and different traverse speeds of 100 mm/min (Fig. 12a and b) and 150 mm/min (Fig. 12c and d), respectively. It can be noted that the grain size distribution is very wide for the low-speed weld with a significant fraction for the large ferrite grains (Fig. 12a) with average grain size of 6.64 µm. However, in the case of high traverse speed, welded joints show a narrower grain size distribution with the significant fraction for the small grain sizes (Fig. 12c) with average grain size of 4.5 µm. In terms of misorientation angle distribution, the high traverse speed shows high fractions of LABs and HABs (Fig. 12d), which reflects the fine grain size and the high density of the LABs.

In terms of the texture, Fig. 13 shows the (111), (101) pole figures and orientation distribution function (ODF) sections at $\Phi = 0^{o}$ and 45° for FSS joints welded at a constant rotation rate of 1000 rpm and different traverse speeds of 100 and 150 mm/min, respectively. The PFs mainly show weak texture with maximum of only three times random at the low travel speed (Fig. 13a) and two times random at the high travel speed (Fig. 13b). The simple shear texture components of the BCC metals can be observed from the ODF sections. It should be noted that the texture components are not at their ideal positions due to the rotations of the shear reference frame during FSW and also due to the tapering of the tool pin (Ref 39). In comparison with the strong simple shear texture reported by Rahimi et al. (Ref 33), the texture observed here can be

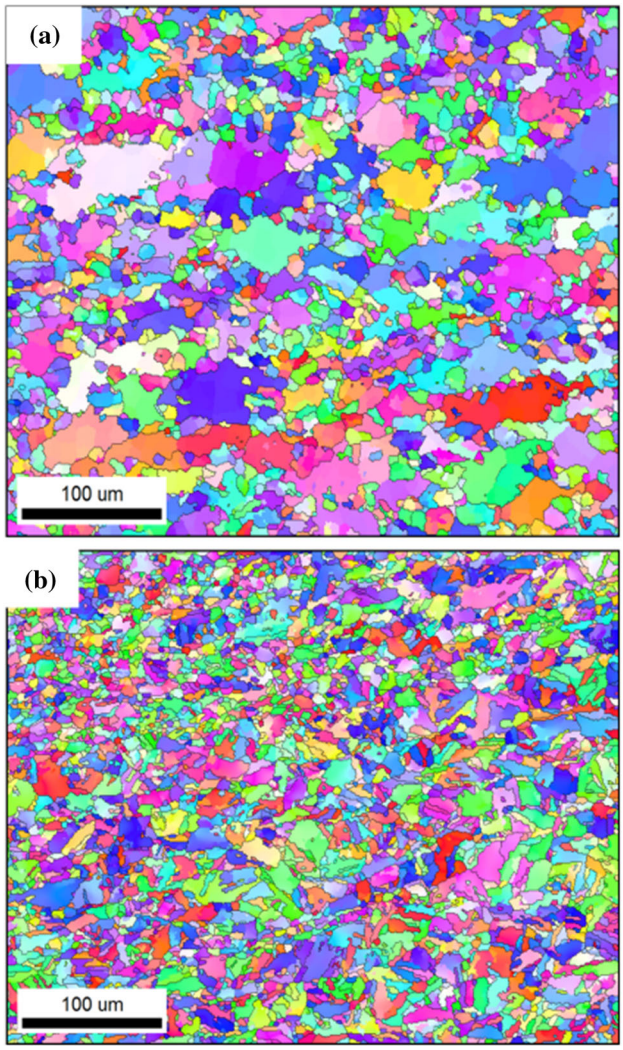

Fig. 10 IPF coloring maps relative to ND of FSWed FSS at rotation rate of 1000 rpm and different traverse speeds of (a) 100 mm/min and (b) 150 mm/min. The IPF coloring triangle is shown in Fig. 3. The EBSD data collected using step size of 1 μm

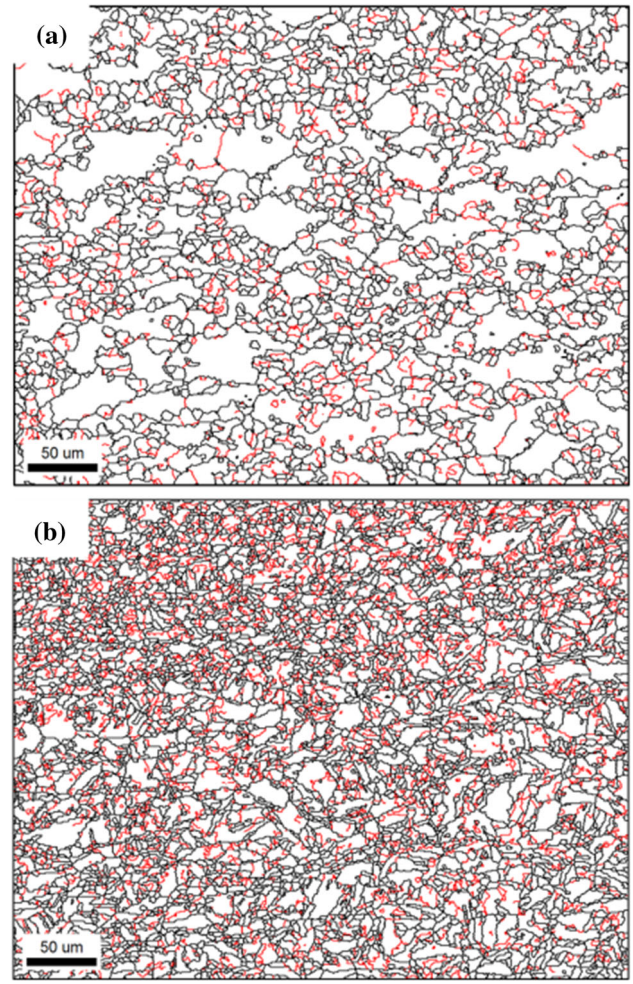

Fig. 11 Grain boundary maps for FSS FSW joints with the HAGBs > 15° in black lines and LABs 5-15° in red lines at rotation rate of 1000 rpm and different traverse speeds of (a) 100 mm/min and (b) 150 mm/min (Color figure online)

considered weak texture. This can be attributed to the difference in the chemical composition of the alloys and also to the difference in the FSW parameters.

The obtained microstructure is further investigated by acquiring high-resolution EBSD data at 0.25 μm from the center of the stir zone of the three joints (Fig. 14) and individual EBSD data at 0.05 μm from the high rotational rate and traverse speed joint (Fig. 15). These high-resolution data are mainly acquired for accurate grain size analysis and are presented as IPF coloring maps and grain boundary maps. The maps clearly show the dual-phase structure obtained in the stir zone of the FSWed FSS joints where the relative proportion between the bainitic and the ferritic grains varies with the FSW parameters. In addition, the size of the ferritic grains also varied with the FSW parameters. The largest grains can be observed in NG zone of the 1000-rpm-100-mm/min joint (Fig. 14a). Increasing the traverse speed to 150 mm/min at the same rotation rate reduces the size of the bainitic and ferritic grains (Fig. 14b). On the other hand, increasing both the welding and the rotation rates results in a significant reduction in the grain size (Fig. 14c), taking into account the variation in the size and distribution of the bainitic/ferritic grain structure within each NG zone through the thickness as observed in the OM microstructure above. For the quantitative analysis of the grain structure, the grain size distribution calculated for the EBSD data is shown in Fig. 14, 15, and 16. It can be observed that the average grain size ranges between 1.7 and 3 μm depending on the FSW parameters, as given in Fig. 16(c) and (b), respectively. From the average grain size values shown in Fig. 16, it can be noted that increasing the rotation rate from 1000 to 1500 rpm at the constant traverse speed of 150 mm/min has resulted in a reduction in the average grain size from 3 to 1.7 μm. This can be attributed to the high amount of strain experienced at the high rotation rate which significantly reduced the grain size. Although there is a clear effect for the FSW parameters on the grain size distribution and the average

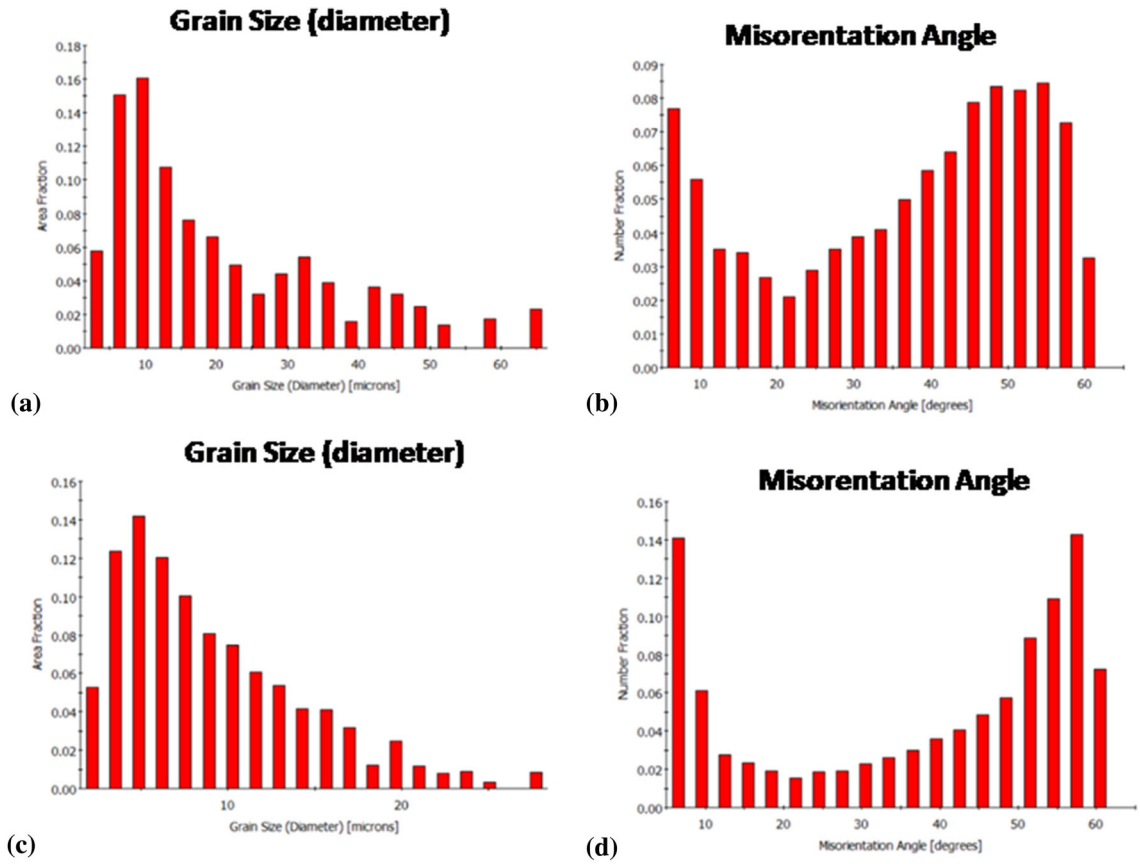

Fig. 12 Grain size distribution and misorientation angle distribution calculated from the data presented in Fig. 10 for FSWed FSS at a constant rotation rate of 1000 rpm and different traverse speeds of (a and b) 100 mm/min and (c and d) 150 mm/min

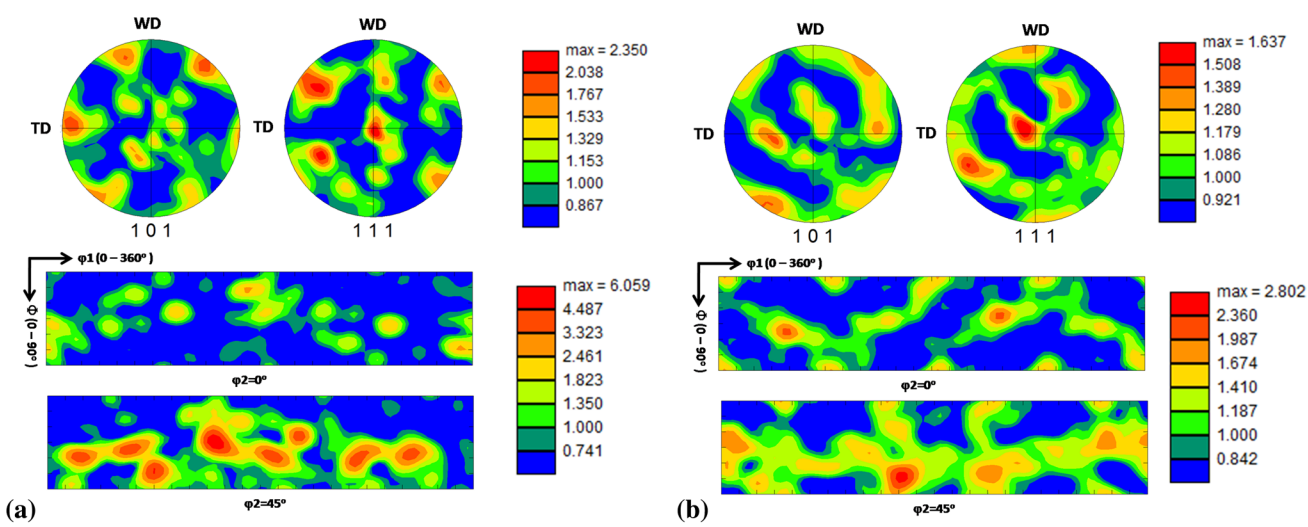

Fig. 13 110, 111 pole figures and ODF sections at Φ = 0° and 45° calculated from the data presented in Fig. 10 for FSWed FSS at a constant rotation rate of 1000 rpm and different traverse speeds of (a) 100 mm/min and (b) 150 mm/min

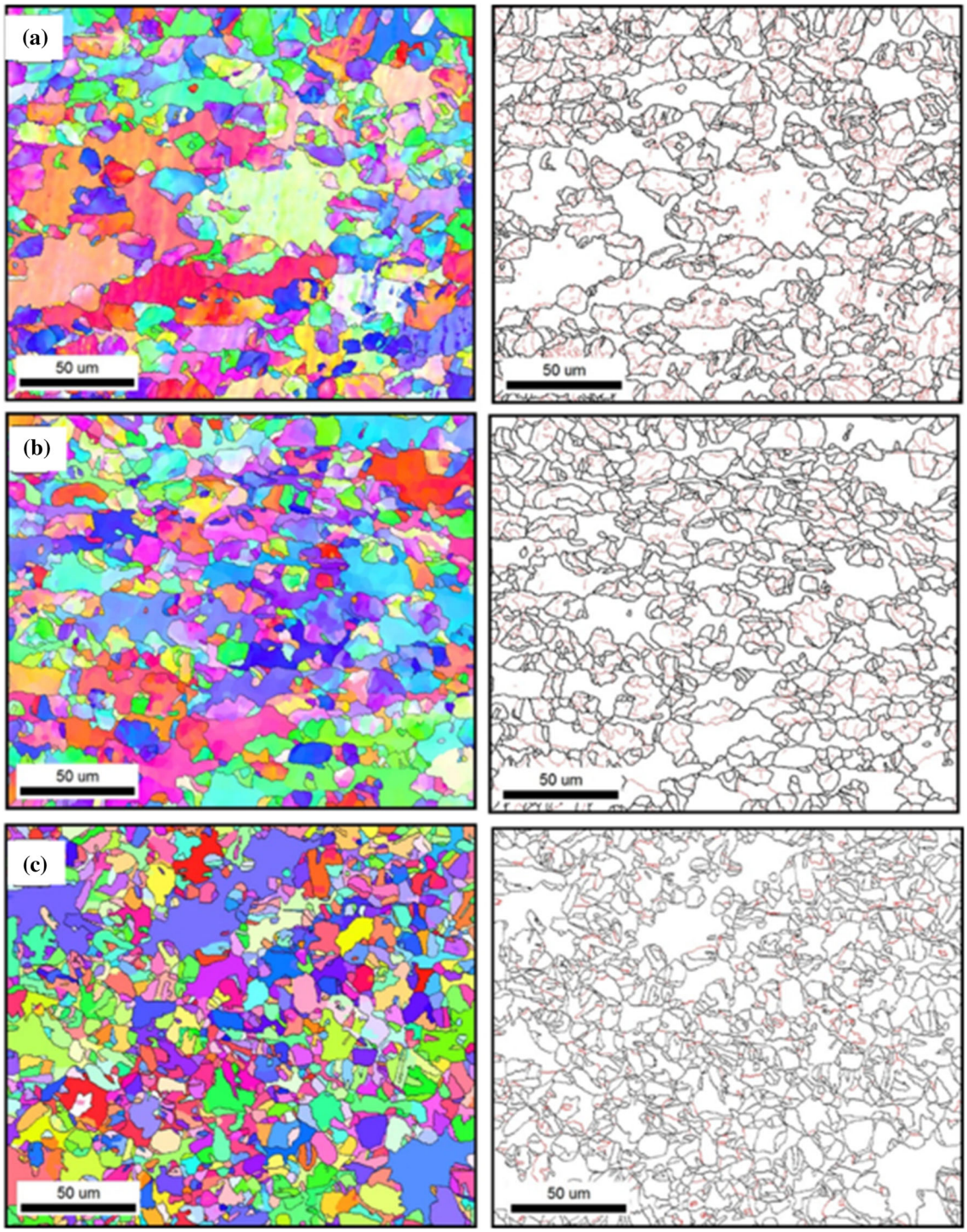

Fig. 14 High-resolution IPF coloring maps relative to ND with their associated grain boundary maps acquired using 0.25-μm step size at the center of the stir zone of FSWed FSS at (a) 1000 rpm—100 mm/min, (b) 1000 rpm—150 mm/min, and (c) 1500 rpm—150 mm/min. IPF coloring triangle is shown in Fig. 3

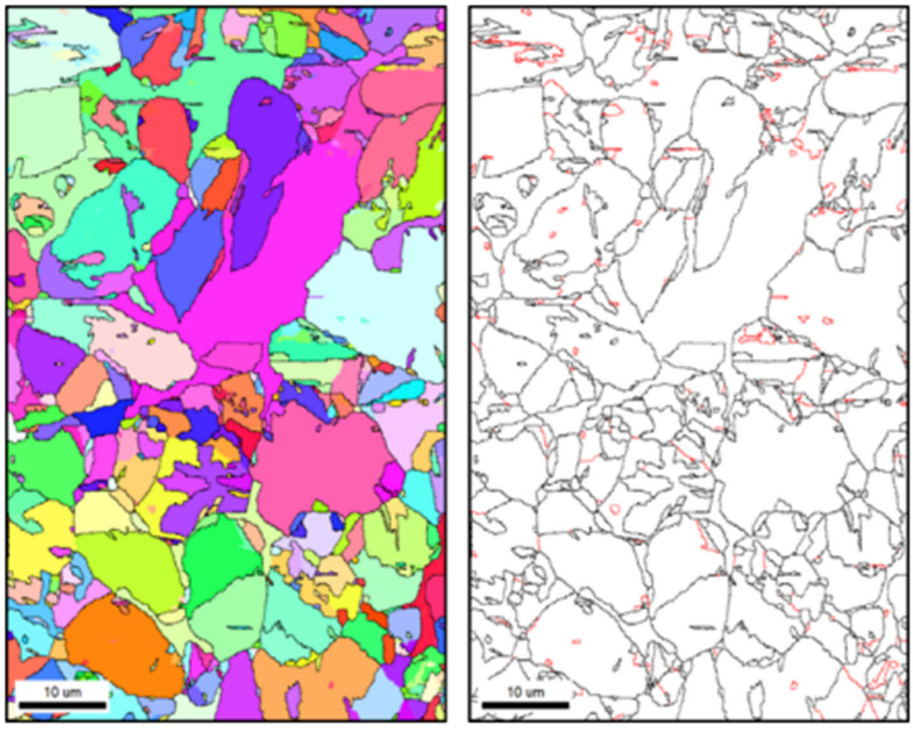

Fig. 15 High-resolution IPF coloring map relative to ND with their associated grain boundary map acquired using 0.05-μm step size at the center of the stir zone of the FSWed FSS joint at 1500 rpm—150 mm/min. IPF coloring triangle is shown in Fig. 3

grain size, the difference is not significant taking into account the through thickness variations. It has been noted that reducing the step size resulted in a decrease in the average grain size. For example, Fig. 15 shows the map obtained using 0.05-μm step size which gives an average grain size of 0.44 μm (Fig. 16d), while the map obtained from the same FSW at 0.25-μm step size gives 1.7 μm of average grain size (Fig. 16c). This means that the microstructure contains ultimately fine grains that can be captured at very small step size such as 0.05 μm. The formation of the fine and ultrafine ferrite grains can be due to the continuous dynamic recrystallization during the high temperature and high shear deformation taking place during FSW (Ref 33).

3.2.3 Mechanical Properties. Tensile test results of the BM as well as the FSWed joints are shown in Fig. 17. The yield strength of the welded samples is lower than the BM, and almost similar tensile strength of the BM is obtained in the FSWed samples. For a constant rotational rate of 1000 rpm, increasing the traverse speed from 100 to 150 mm/min decreases both the yield strength and the ultimate tensile strength. For constant traverse speed of 150 mm/min, increasing rotational rate from 1000 to 1500 rpm does not affect the mechanical properties. However, about 50% reduction in the ductility of the FSWed materials is obtained for conditions. All the tensile specimens of FSW joints failed outside the weld zone as shown in Fig. 18 which shows the tensile specimen fracture locations. This may explain the lower yield strength and ductility since failures occur in the HAZ. Further examinations of tensile behaviors of the FSWed FSS joints were conducted by observing the fracture surfaces of the failed tensile samples using SEM as given in Fig. 19. It should be noted that as a result of all tensile samples failed in the BM, nearly the same failure patterns are observed. Thus, the topographic features of the failed FSWed materials look the same as those of the as-received FSS BM (Fig. 19a, b, and c). Deep and shallow dimples are the main features indicating the ductile mode of failure (Ref 38). Some porosity and microcracks are also observed on the fracture surfaces of all the failed specimens.

Hardness measurements conducted at the midsection of the transverse cross section of the weld zone and the hardness profiles are illustrated in Fig. 20. It can be observed that for all FSW conditions, the hardness increases from 190 Hv in the base material to an average of 330 Hv in the weld zone. This

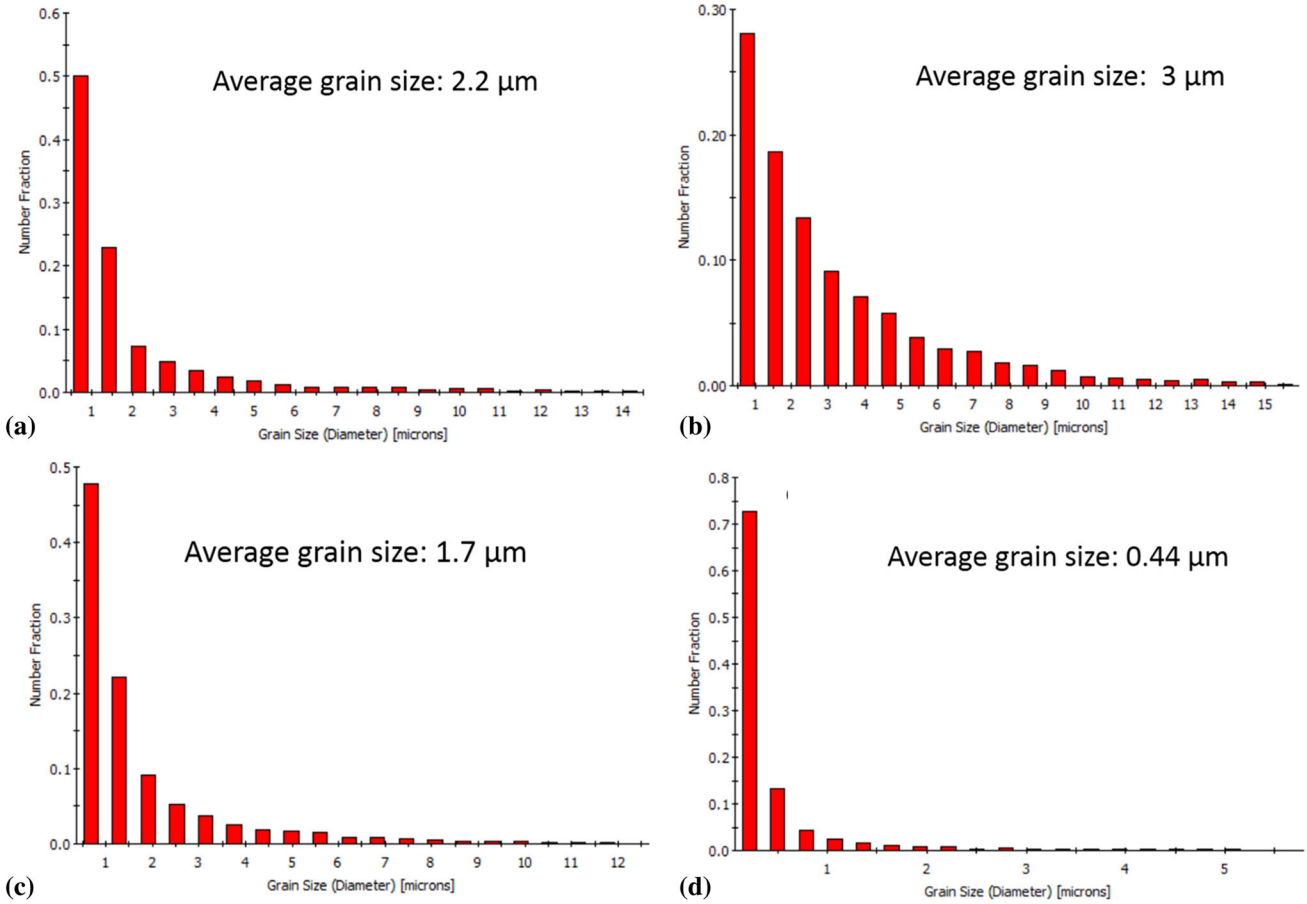

Fig. 16 Grain size distributions calculated from the EBSD data presented in Figs. 14 and 15 (a) 1000 rpm—100 mm/min, (b) 1000 rpm—150 mm/min, (c) 1500 rpm—150 mm/min (all data collected at 0.25 µm), and (d) 1500 rpm—150 mm/min (data collected at 0.05 µm)

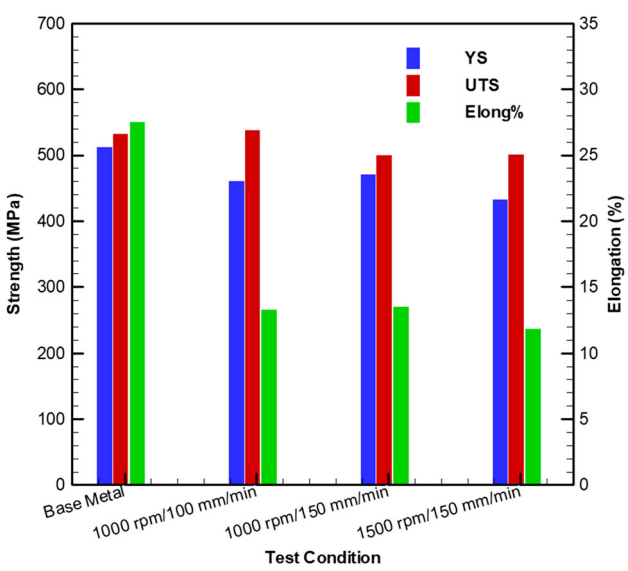

Fig. 17 Yield strength, ultimate tensile strength and elongation for the FSS joints in comparison with BM

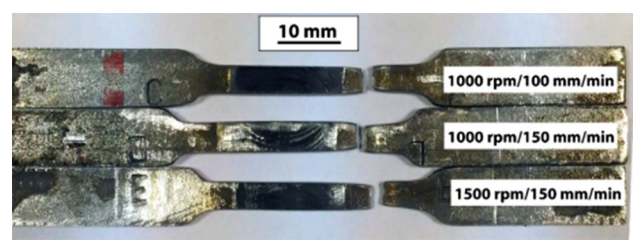

Fig. 18 An image for the tensile test specimens of the FSWed FSS AISI 409 showing the failure locations

can be attributed to the fine and ultrafine bainitic/ferritic grains obtained in the NG zone after FSW. The hardness values varied with the average grain size roughly according to $Hv = \frac{10.76}{\sqrt{d}} + 92.57$, where d is the average grain size, but with a low correlation coefficient (R2 = 0.7374) presumably due to a large variation in the grain size. The Hall–Petch correlation for the yield strength could not be developed since failure occurred outside weld zone.

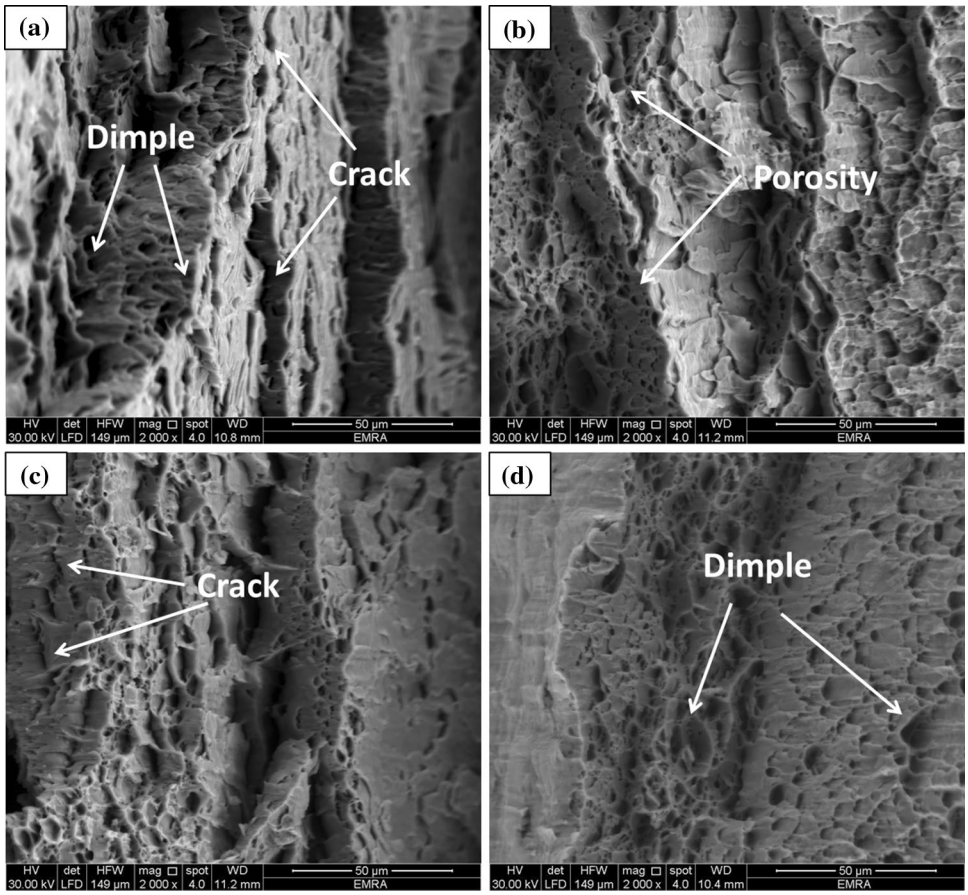

Fig. 19 Fracture surface SEM micrographs of (a) as-received FSS and the FSWed FSS joints at (b) 1000 rpm, 100 mm/min, (c) 1000 rpm, 150 mm/min, and (d) 1500 rpm, 150 mm/min

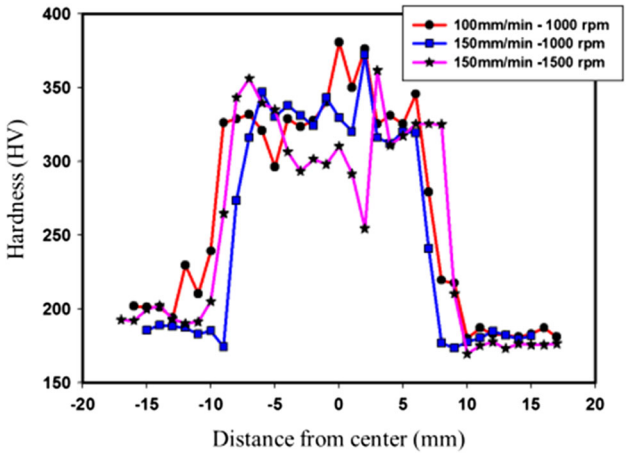

Fig. 20 Hardness measurements of the FSWed FSS joints at different rotational and traverse speeds

The reduction in the ductility of the FSW joints can be attributed to the significant increase in the hardness and the significant reduction in the grain size to the extent of submicron. These factors make the weld region of high strength, and hence, the tensile samples failed in the BM part of the gauge length.

4. Conclusions

Friction stir welding has been used successfully to produce sound butt joints in 4-mm-thick plates of AISI 409 FSS at different rotational and traverse speeds. The joints were characterized using OM, SEM, EBSD, tensile and hardness tests, and the following conclusions can be drawn:

1. During FSW of the FSS AISI 409, the deformation process took place in the austenite/ferrite phase field that transformed upon cooling into bainitic/ferritic microstructure.
2. The relative fractions between the bainitic and ferritic phases varied through the thickness of the weld zone and also varied with the FSW parameters.
3. The fraction and size of the ferrite phase decreased toward the bottom of the weld zone and increased by the increase in the FSW parameters.
4. Significant grain size reduction had been obtained in the NG zone up to the submicron level.
5. Almost the ultimate tensile strength of the base materials had been retained in the FSWed joints with some reduction in the ductility that attributed to the enhanced strength of the weld zone.

6. The hardness at the FSWed zone had been improved by about 74% relative to the base material due the significant grain size reduction and the mixture of the bainitic/ferritic microstructure.
7. The crystallographic texture resembled the BCC metals' simple shear texture that of weak intensity to the extent that can be considered random in some cases.

References

1. J. Charles, J.-D. Mithieux, P.O. Santacreu, and L. Peguet, The Ferritic Stainless Family: The Appropriate Answer to Nickel Volatility?, *Rev. Métallurgie*, 2009, **106**, p 124–139
2. G. Sharma and D.K. Dwivedi, Study on Microstructure and Mechanical Properties of Dissimilar Steel Joint Developed Using Friction Stir Welding, *Int. J. Adv. Manuf. Technol.*, 2017, **88**, p 1299–1307
3. M. Mondal, H. Das, E.Y. Ahn, S.T. Hong, M.-J. Kim, H.N. Han, and T.K. Pal, Characterization of Friction Stir Welded Joint of Low Nickel Austenitic Stainless Steel and Modified Ferritic Stainless Steel, *Met. Mater. Int.*, 2017, **23**(5), p 948–957
4. J.-H. Schmitt, Some Examples of Stainless Steel Use in the Automotive Industry, *Key Eng. Mater.*, 2002, **230-232**, p 17–22
5. J.C. Villafuerte and H.W. Kerr, Grain Structures in Gas Tungsten-Arc Welds of Austenitic Stainless Steels with Ferrite Primary Phase, *Metall. Trans. A*, 1990, **21**, p 979–986
6. X. Lei, Y. Deng, Y. Peng, Z. Yin, and G. Xu, Microstructure and Properties of TIG/FSW Welded Joints of a New Al-Zn-Mg-Sc-Zr Alloy, *J. Mater. Eng. Perform.*, 2013, **22**(9), p 723–2729
7. M.M.Z. Ahmed, B.P. Wynne, and J.P. Martin, Effect of Friction Stir Welding Speed on Mechanical Properties and Microstructure of Nickel Based Super Alloy Inconel 718, *Sci. Technol. Weld. Join.*, 2013, **18**(8), p 680
8. ARSh Essa, M.M.Z. Ahmed, A.Y.A. Mohamed, and A.E. El-Nikhaily, An Analytical Model of Heat Generation for Eccentric Cylindrical Pin in Friction Stir Welding, *J. Mater. Res. Technol.*, 2016, **5**(3), p 234–240
9. S. Khodir, M.M.Z. Ahmed, S. Mohamed, E. Ahmed, and H. Abdelaleem, Effect of Intermetallic Compound Phases on the Mechanical Properties of the Dissimilar Al/Cu Friction Stir Welded Joints, *J. Mater. Eng. Perform.*, 2016, **25**(11), p 4637–4648
10. F.C. Liu and T.W. Nelson, In-situ Grain Structure and Texture Evolution During Friction Stir Welding of Austenite Stainless Steel, *Mater. Des.*, 2017, **115**, p 467–478
11. M.M.Z. Ahmed, B.P. Wynne, M.M. Seleman, and W.M. Rainforth, A Comparison of Crystallographic Texture and Grain Structure Development in Aluminum Generated by Friction Stir Welding and High Strain Torsion, *Mater. Des.*, 2016, **103**, p 259–267
12. G.K. Padhy, C.S. Wu, and S. Gao, Friction Stir Based Welding and Processing Technologies—Processes, Parameters, Microstructures and Applications: A Review, *J. Mater. Sci. Technol.*, 2018, **34**(1), p 1–38
13. F.C. Liu, Y. Hovanski, M.P. Miles, C.D. Sorensen, and T.W. Nelson, A Review of Friction Stir Welding of Steels: Tool, Material Flow, Microstructure, and Properties, *J. Mater. Sci. Technol.*, 2018, **34**(1), p 39–57
14. A.S. Hamada, A. Järvenpää, M.M.Z. Ahmed, M. Jaskari, B.P. Wynne, D.A. Porter, and L.P. Karjalainen, Microstructural Evolution of Friction-Stir-Welded AA6082-T6 Aluminum Alloy during Cyclic Deformation, *Mater. Sci. Eng. A*, 2015, **642**, p 366–376
15. A. Barbini, J. Carstensen, and J.F. dos Santos, Influence of a Non-rotating Shoulder on Heat Generation, Microstructure and Mechanical Properties of Dissimilar AA2024/AA7050 FSW Joints, *J. Mater. Sci. Technol.*, 2018, **34**(1), p 119–127
16. W. Han, P. Liu, X. Yi, Q. Zhan, F. Wan, K. Yabuuchi, H. Serizawa, and A. Kimura, Impact of Friction Stir Welding on Recrystallization of Oxide Dispersion Strengthened Ferritic Steel, *J. Mater. Sci. Technol.*, 2018, **34**(1), p 209–213
17. G. Chena, Q. Ma, S. Zhanga, J. Wua, G. Zhanga, and Q. Shi, Computational Fluid Dynamics Simulation of Friction Stir Welding: A Comparative Study on Different Frictional Boundary Conditions, *J. Mater. Sci. Technol.*, 2018, **34**(1), p 128–134
18. S.S. Kumar, N. Murugan, and K.K. Ramachandran, Microstructure and Mechanical Properties of Friction Stir Welded AISI, 316L Austenitic Stainless Steel Joints, *J. Mater. Process. Technol.*, 2018, **254**, p 79–90
19. H. Li, S. Yang, S. Zhang, B. Zhang, Z. Jiang, H. Feng, P. Han, and J. Li, Microstructure Evolution and Mechanical Properties of Friction Stir Welding Super-Austenitic Stainless Steel S32654, *Mater. Des.*, 2017, **118**, p 207–217
20. Y.-G. Miao, G.-Y. Chen, P. Zhang, and D.-F. Han, Comparative Study of Bypass-Current MIG Welded-Brazed Aluminum/Galvanized Steel and Aluminum/Stainless Steel, *Acta Metall. Sin. (Engl. Lett.)*, 2017, **30**(8), p 721–730
21. X. Liu, H. Liu, T. Wang, X. Wang, and S. Yang, Correlation Between Microstructures and Mechanical Properties of High-Speed Friction Stir Welded Aluminum Hollow Extrusions Subjected to Axial Forces, *J. Mater. Sci. Technol.*, 2018, **34**(1), p 102–111
22. M.M.Z. Ahmed, S. Ataya, M.M. El-Sayed Seleman, H.R. Ammar, and E. Ahmed, Friction Stir Welding of Similar and Dissimilar AA7075 and AA5083, *J. Mater. Process. Technol.*, 2017, **242**, p 77–91
23. H.-H. Cho, H.N. Han, S.-T. Hong, J.-H. Park, Y.-J. Kwon, S.-H. Kim, and R.J. Steel, Microstructural Analysis of Friction Stir Welded Ferritic Stainless Steel, *Mater. Sci. Eng. A*, 2011, **528**(6), p 2889–2894
24. M.B. Bilgin, C. Meran, and O.E. Canyurt, Effect of Tool Angle on Friction Stir Weldability of AISI, 430, *Weld. J.*, 2013, **92**, p 42–46
25. W.M. Thomas, C.S. Wiesner, D.J. Marks, and D.G. Staines, Conventional and Bobbin Friction Stir Welding of 12% Chromium Alloy Steel Using Composite Refractory Tool Materials, *Sci. Technol. Weld. Join.*, 2009, **14**(3), p 247–253
26. A.K. Lakshminarayanan and V. Balasubramanian, Understanding the Parameters Controlling Friction Stir Welding of AISI, 409M Ferritic Stainless Steel, *Met. Mater. Int.*, 2011, **17**(6), p 969–981
27. A.K. Lakshminarayanan and V. Balasubramanian, Assessment of Fatigue Life and Crack Growth Resistance of Friction Stir Welded AISI, 409M Ferritic Stainless Steel Joints, *Mater. Sci. Eng. A*, 2012, **539**, p 143–153
28. A. Salemi Golezani, S.M. Arab, S. Javadi, and F. Kargar, The Effect of Friction Stir Processing Speed Ratio on the Microstructure and Mechanical Properties of A 430 Ferritic Stainless Steel, *J. Adv. Mater. Process.*, 2014, **2**(2), p 39–48
29. J. Han, H. Li, Z. Zhu, F. Barbaro, L. Jiang, H. Xu, and L. Ma, Microstructure and Mechanical Properties of Friction Stir Welded 18Cr–2Mo Ferritic Stainless Steel Thick Plate, *Mater. Des.*, 2014, **63**, p 238–246
30. M.B. Bilgin and C. Meran, The Effect of Tool Rotational and Traverse Speed on Friction Stir Weldability of AISI, 430 Ferritic Stainless Steels, *Mater. Des.*, 2012, **33**, p 376–383
31. M.M.Z. Ahmed, E. Ahmed, A.S. Hamada, S.A. Khodir, M.M. El-Sayed Selema, and B.P. Wynne, Microstructure and Mechanical Properties Evolution of Friction Stir Spot Welded High-Mn Twinning-Induced Plasticity Steel, *Mater. Des.*, 2016, **91**, p 378–387
32. H.K.D.H. Bhadeshia and R.W.K. Honeycombe, *Steels: Microstructure and Properties*, 3rd ed., Butterworth-Heinemann, Oxford, 2006
33. S. Rahimi, B.P. Wynne, and T.N. Baker, Development of Microstructure and Crystallographic Texture in a Double-Sided Friction Stir Welded Microalloyed Steel, *Metall. Mater. Trans. A*, 2017, **48**, p 362–378
34. D. Wang, D.R. Ni, B.L. Xiao, Z.Y. Ma, W. Wang, and K. Yang, Microstructural Evolution and Mechanical Properties of Friction Stir Welded Joint of Fe-Cr-Mn-Mo-N Austenite Stainless Steel, *Mater. Des.*, 2014, **64**, p 355–359
35. H.B. Li, Z.H. Jiang, H. Feng, S.C. Zhang, L. Li, P.D. Han, R.D.K. Misra, and J.Z. Li, Microstructure, Mechanical and Corrosion Properties of Friction Stir Welded High Nitrogen Nickel-Free Austenitic Stainless Steel, *Mater. Des.*, 2016, **84**, p 291–299
36. J.J. Jeon, S. Mironov, Y.S. Sato, H. Kokawa, S.H.C. Park, and S. Hirano, Grain Structure Development During Friction Stir Welding of Single-Crystal Austenitic Stainless Steel, *Metall. Mater. Trans. A*, 2013, **44**(7), p 3157–3166
37. M. Mahmoudiniya, A.H. Kokabi, S. Kheirandish, and L.A.I. Kestens, Microstructure and Mechanical Properties of Friction Stir Welded Ferrite Martensite DP700 Steel, *Mater. Sci. Eng., A*, 2018, **737**, p 213–222

38. A.K. Lakshminarayanan and V. Balasubramanian, An Assessment of Microstructure, Hardness, Tensile and Impact Strength of Friction Stir Welded Ferritic Stainless Steel Joints, *Mater. Des.*, 2010, **31**(10), p 4592–4600
39. M.M.Z. Ahmed, B.P. Wynne, W.M. Rainforth, A. Addison, J.P. Martin, and P.L. Threadgill, Effect of Tool Geometry and Heat Input on the Hardness, Grain Structure, and Crystallographic Texture of Thick-Section Friction Stir-Welded Aluminium, *Metall. Mater. Trans. A*, 2019, **50A**, p 271–284

Publisher's Note Springer Nature remains neutral with regard to jurisdictional claims in published maps and institutional affiliations.